IEEE Access
Multidisciplinary | Rapid Review | Open Access Journal

Received March 5, 2021, accepted March 17, 2021, date of publication March 22, 2021, date of current version April 8, 2021.

Digital Object Identifier 10.1109/ACCESS.2021.3067728

The Calculation Method of PV Direct Current Energy Based on Modulated Broadband Mode Decomposition and Compound Simpson Integral Algorithm

Z. C. WANG[1], Y. F. PENG[1], (Member, IEEE), Y. F. LIU[2], K. F. HE[3], Z. T. WU[2], AND B. Q. LI[2]

[1]Hunan Provincial Key Laboratory of Health Maintenance for Mechanical Equipment, Hunan University of Science and Technology, Xiangtan 411201, China
[2]College of Mechanical and Vehicle Engineering, Hunan University, Changsha 410082, China
[3]School of Mechatronics Engineering, Foshan University, Foshan 528000, China

Corresponding author: Y. F. Peng (hnkjdxhkfpyf@sina.com)

This work was supported in part by the National Key Research and Development Program of China under Grant 2018YFF0212902 and Grant 2018YFB130800, in part by the National Natural Science Foundation of China under Grant 51805161, in part by the Research Project of Hunan Provincial Department of Education under Grant 19C0769, in part by the Guangdong Provincial Natural Science Foundation of China under Grant 2019A1515011961, in part by the Hunan Provincial Natural Science Foundation of China under Grant 2018JJ3182, and in part by the Scientific Research Fund of Hunan Provincial Education Department under Grant 19B191.

ABSTRACT The application of photovoltaic power is becoming more and more extensive presently, when the existing time-frequency analysis methods are used to analyze photovoltaic mutation signals such as transient rise and transient fall, the cornered signal will produce Gibbs phenomenon and leads to errors. Thus, the Broadband Mode Decomposition (BMD) method is proposed. The main idea of BMD is to search in the associated dictionary that contains the wideband and narrowband signals. However, the BMD algorithm may treat the wideband signal as several narrowband components, when applied to a wideband signal interfered by strong noise, because the relative bandwidth is not sufficiently small. Therefore, a modulated broadband modal decomposition (MBMD) based on the modulation differential operator is proposed. By multiplying a high-frequency single-frequency signal, the relative bandwidth of the effective wideband signal is much smaller than 1, and the wideband signal is processed as an approximate wideband signal. Meanwhile, because the errors of the traditional dot product sum algorithm in DC energy measurement cannot be positive and negative offset, while the compound Simpson integral algorithm has small error and high calculation accuracy. Therefore, a photovoltaic DC power calculation method based on the MBMD and compound Simpson integration is proposed.

INDEX TERMS Modulated broadband mode decomposition algorithm, compound Simpson integral algorithm, photovoltaic direct current power measurement, modulated difference operator.

I. INTRODUCTION

The application of photovoltaic power generation is increasingly widespread. The solar photovoltaic power generation industry is in a stage of rapid development. The extensive use of various DC power electronic equipment such as rectifiers, inverters, frequency converters, and charging piles in photovoltaic power generation DC systems has brought considerable economic benefits. However, due to the nonlinearity, impact and imbalance of the load, these equipment can increase various disturbance components in the power grid, which may cause power quality problems such as ripple, distortion, and noise in the power grid. These power quality problems will seriously affect the stability of the power supply network and the use of electrical appliances [1]–[5]. Since most voltages in home circuits are AC voltage, the research on AC power has been in progress, and the AC power measurement method has been developed to be relatively mature. However, the DC power measurement method is not sufficiently mature, so research for a photovoltaic DC power measurement method is of great significance [6], [7].

The associate editor coordinating the review of this manuscript and approving it for publication was Xiaofeng Yang.

In engineering fields, many time-frequency analysis methods are used to extract features from noise signals [8]–[15]. These adaptive time-frequency analysis methods can be divided into two types: methods based on Fourier transform and methods not based on Fourier transform [16], [17]. The methods based on Fourier transform include wavelet transform (WT) and variational modal decomposition (VMD) methods. These methods that achieve signal decomposition are based on frequency domain calculations [18]. K. Dragomiretskiy and D. Zosso proposed the VMD method, which is an adaptive filter based on multiple Wiener filters [18]. It has been proven that compared to the previous methods, VMD shows good performance in the analysis of complex nonstationary signals [19]–[21]. The methods that are not based on Fourier transform are the ensemble empirical mode decomposition (EEMD), empirical mode decomposition (EMD), and local mode decomposition (LMD), which calculate the envelope of the extreme point and decompose the original signal into several intrinsic mode functions [22]. Z. Wu *et al.* proposed the EEMD, by adding different levels of white noise to the original signal, and averaging the decomposition results, which improved the anti-noise ability of EMD [23]. Recent studies have shown that the VMD and EEMD methods are superior and effective [24], [25], so they are selected as representatives of Fourier transform-based methods and non-Fourier transform-based methods to compare with the proposed methods.

In the photovoltaic DC signal, due to the input and output of the DC linear load, a disturbance signal with sharp corners similar to a square wave signal will be generated. The existing time-frequency analysis methods have problems with ''sharp edges'' signals such as sawtooth signals and square wave signals, because their frequency bands are infinite [26], which can be considered broadband signals.

First, for the method based on Fourier transform, the essence of the algorithm is multiscale adaptive filtering. However, Gibbs phenomenon shows that after filtering [27], the high-frequency part of the broadband signal will attenuate or disappear, which may cause a series of interference at the breakpoint of the decomposition result. Second, for the method that is not based on Fourier transform, the envelope of the extreme point is calculated by the interpolation function, and the original signal is divided into various ''smooth'' narrow-band intrinsic mode functions (IMFs). Hence, errors will inevitably occur when addressing the broadband components. Therefore, the Broadband Mode Decomposition (BMD) algorithm [16], [17] is proposed. An association dictionary containing common wideband data (such as square wave, sawtooth and narrowband data) is constructed in the BMD algorithm. Then, using optimization methods to get the sparse solutions, by searching in the association dictionary. The BMD method uses the regulating differential operator as the best object. For noisy nonstationary signals, BMD is suitable for extracting wideband and narrowband features, which compared with previous signal decomposition algorithms. However, the BMD algorithm may treat the wideband signal as several narrowband components, when applied to wideband signals that are interfered by strong noise [28], because the relative bandwidth is not sufficiently small. Therefore, this paper proposes a broadband modal decomposition (MBMD) method based on modulation differential operator to denoise photovoltaic DC signals. By multiplying the high-frequency single-frequency signal, the effective wideband signal's relative bandwidth is converted to much less than 1, and the wideband signal is considered an approximate wideband signal to obtain a more accurate decomposition result.

Simpson integration algorithm [29]–[33] is a common integration algorithm, which was created by the Englishman Thomas Simpson, where the numerical approximation solution of a definite integral is obtained by the method of quadratic curve approximation. Simpson algorithm has a wide range of applications in medicine, mathematics, electronics, machinery, information, etc., but it is rarely used in photovoltaic DC power measurement. In this paper, MBMD algorithm is used to decompose signals and extract features, then, the compound Simpson integral algorithm is used to measure the DC energy. In the following, simulation and experiment will demonstrate the effectiveness of this method.

The remainder of the paper is as follows. Section 2 introduces the theory MBMD signal decomposition algorithm and compound Simpson integral algorithm, and establishes a mathematical model. Section 3 verifies the correctness of the theory through simulation signal. Section 4 analyzes the measured data. Section 5 provides the conclusion.

II. THEORETICAL ANALYSIS

A. PHOTOVOLTAIC DC SIGNAL MODELING

The DC signal in the photovoltaic system has disturbances. Therefore, a photovoltaic direct current signal model can be established here for some common disturbances of direct current signals. In the next chapter, the established signal model will be simulated and analyzed by MATLAB. The following model is constructed for the transient rise, transient fall, harmonics and other disturbances that often occur in DC signals:

First, a signal S with DC components, harmonics (because the harmonics generated in the photovoltaic DC circuit are mainly second harmonics, so the harmonics constructed here are second harmonics) and noise is constructed.

Then, a signal model S_1 with a signal with transient rise and transient fall are constructed. Because there are linear and nonlinear loads in the circuit, which have different signal waveforms when they are connected to and disconnected from the circuit, there is a buffering process for nonlinear loads. The linear load is a process where the current directly changes to the corresponding position when it is connected or disconnected without buffering. To reflect the difference between the two types of loads, the swell and sag signal of the nonlinear load is added to signal S_1.

Based on signal S_1, the swell and sag signal of the linear load is added to form the new model S_2.

$$S_2 = \underbrace{u_0(t)}_{\text{DC signal}} + \underbrace{\sum_k A_k u_k(t)}_{\text{Harmonic signal}} + \underbrace{\sum_i A_i u_i(t)}_{\substack{\text{Linear load transient rise} \\ \text{and transient fall signal}}} + \underbrace{\sum_j A_j u_j(t)}_{\substack{\text{Non-linear load transient rise} \\ \text{and transient fall signal}}} + \underbrace{x(n)}_{\text{Noise signal}} \quad (1)$$

In the above formula, $u_0(t)$ is the DC component in the mixed signal S_2, $u_k(t)$, $u_i(t)$ and $u_j(t)$ are the disturbance components, A_k, A_i and A_j are their respective coefficients, $x(n)$ is the noise signal.

B. MBMD SIGNAL DECOMPOSITION

The definition of the narrowband signal is as follows [24]:

$$x_{narrow}(t) = A(t)\cos(\omega t + \phi(t)) \quad (2)$$

$A(t)$ is limited by the frequency band, and its center frequency ω' is much smaller than ω, $\phi(t)$ is a slowly changing function. The relative bandwidth is $2\omega'/\omega$,and it is much less than 1.

In Equation (2) the BMD adjustment difference operator can effectively distinguish narrowband signals from noise, because the operator can express the smoothness of non-stationary signals, and narrowband or broadband signals are always smoother than noise. In the BMD method, to constrain the generated component to make it smoother than the original signal, an adjustable difference operator is constructed. Although for narrowband signals, this operator is applicable, it can be applied to wideband signals too.

For wideband signals, pulse signals such as sawtooth signals and square wave signals with ''sharp corners'' are wideband signals, because their frequency bands are infinite [20]. The Fourier series of the square wave signal and sawtooth signal are as follows:

$$square(t) = \sum_{i=1}^{+\infty} \frac{1}{2i-1} \sin\left[(2i-1)t\right] \quad (3)$$

$$sawtooth(t) = \sum_{i=1}^{+\infty} \frac{(-1)^{(i-1)}}{(2i-1)^2} \sin\left[(2i-1)t\right] \quad (4)$$

According to Equation (3) and Equation (4), the amplitude of the sinusoidal component decreases when the frequency increases. Therefore, the general form of the broadband signal can be constructed:

$$x_{broad}(t) = \sum_{i=1}^{+\infty} A_i \sin\left[i\omega t + \theta_i(t)\right] \quad (5)$$

A_i decreases with the increase in ω. When $\omega \to \infty, A \to 0$ and $\theta(t)$ slowly change.

Although the wideband signal's frequency is a multiple of the narrowband signal in Equation (5), because the frequency amplitude rapidly decreases, the wideband signal is still smoother than the noise signal, which can distinguish the wideband signal from the noise. However, there are problems with wideband signals, because for narrowband signals, the modulation differential operator was designed originally. For $x_{narrow}(t)$, the theoretically generated component is using an envelope $A(t)/A$ to multiply the first Fourier series $A\cos(\omega t + \phi(t))$, and in the narrowband signal, there is only one dominant frequency ω.

However, in $x_{broad}(t)$, there are multiple main frequencies with different amplitudes. For example, $A_{i-1}\sin[(i+1)\omega t + \theta_{i-1}(t)\ ]$ and $A_i \sin[i\omega t + \theta_i(t)\ ]$. The wideband signal's center frequency is ω, but among the sinusoidal components the frequency interval is also ω. The bandwidth divided by the center frequency is the definition of relative bandwidth, which is $\omega/\omega = 1$. The narrowband signals' relative bandwidth are proved much less than 1 in Equation (2). The BMD algorithm may consider $A_{i-1}\sin\left[(i-1)\omega t + \theta_{i-1}(t)\right]$ and $A_i \sin\left[i\omega t + \theta_i(t)\right]$ as two different components, for wideband signals interfered by strong noise. Because the relative bandwidth is not sufficiently small, and the wideband signal will be divided into several narrowband components.

We will introduce how to construct the modulation differential operator:

$$\begin{aligned} x'_{broad}(t) &= x_{broad}(t)\sin(\omega' t) \\ &= \sum_{i=1}^{+\infty} A_i \sin\left[i\omega t + \theta_i(t)\right]\ \sin(\omega' t) \end{aligned} \quad (6)$$

In the above Equation, M is a preset positive integer, which can usually be set to 5-10, $\sin(\omega' t)$ is a high-frequency single-frequency signal with $\omega' = M\omega$, and $x'_{broad}(t)$ is a modulated signal. Then, $x'_{broad}(t)$ can be converted into the following form:

$$\begin{aligned} x'_{broad}(t) = &\frac{1}{2}\sum_{i=1}^{+\infty} A_i \cos\left[(\omega' - i\omega)t - \theta_i(t)\right] \\ &+ \frac{1}{2}\sum_{i=1}^{+\infty} A_i \cos\left[(\omega' + i\omega)t + \theta_i(t)\right] \end{aligned} \quad (7)$$

The center frequency is moved from ω to $\omega'+\omega$ and $\omega'-\omega$. Thus, the relative bandwidths are $\omega/(\omega'-\omega)$ and $\omega/(\omega'+\omega)$, which are much less than 1. It can be easily proven that the relative bandwidth of a narrowband signal after modulation is much less than 1. Therefore, we can construct the modulation difference operator as follows:

$$\begin{aligned} T_j = &\left\| D^{(2)}\left[IMF_i^j(n)\right]\right\|_2^2 \\ &+ \lambda \left\| D^{(2)}\left[x(n)\sin(\omega' t) - IMF_i^j(n)\right]\right\|_2^2 \end{aligned} \quad (8)$$

Then, based on the modulation difference operator, the broadband mode decomposition algorithm is constructed according to the following steps:

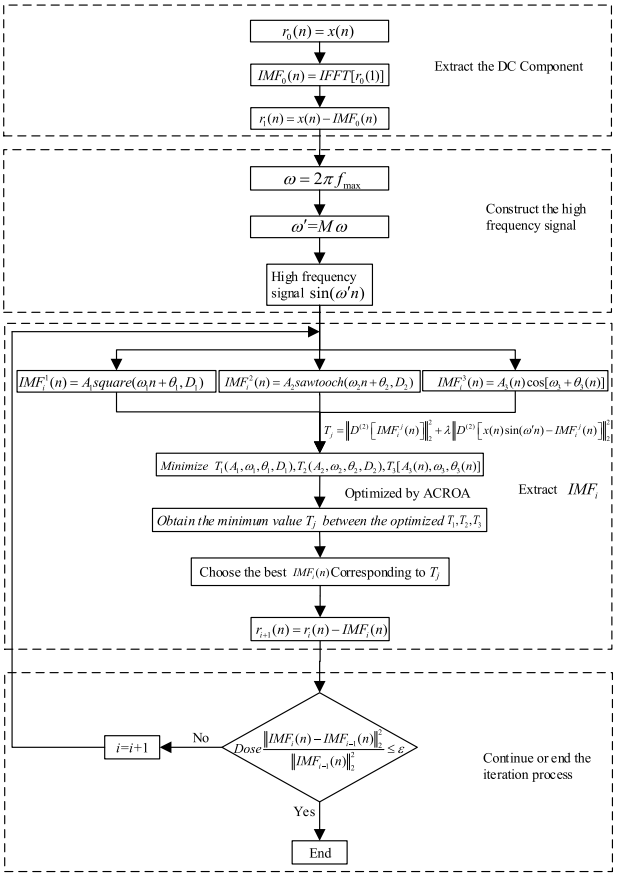

FIGURE 1. The iteration procedure of MBMD.

Based on the modulation differential operator, which is constructed in Equation (8), the main process of MBMD is as follows and the flow chart of MBMD is shown in Figure 1.

(1) Set $r_0(n)$ to be equal to $x(n)$.

(2) Extract direct current (DC) signals from the original signal.

$$IMF_0(n) = ifft[\hat{r}_0(1)] \tag{9}$$

$$r_1(n) = x(n) - IMF_0(n) \tag{10}$$

i is set to 1, $ifft[\hat{r}_0(1)]$ is the IFT of $\hat{r}_0(1)$, and $\hat{r}_0(k)$ is the FT of $r_0(n)$.

(3) Construct the optimal problem P_1 as follows:

$$\begin{aligned} P1: &\ Minimize\ T_1(A_1,\omega_1,\theta_1,D_1),\\ &\ T_2(A_2,\omega_2,\theta_2,D_2),T_3[A_3(n),\omega_3(n),\theta_3(n)]\\ S.T.&\ x(n)=\sum_{i=0}^{N} IMF_i(n)+res(n),\ IMF_i^j\in Dic_j \end{aligned} \tag{11}$$

$$\begin{aligned} T_j = &\left\|D^{(2)}\left[IMF_i^j(n)\right]\right\|_2^2\\ &+\lambda\left\|D^{(2)}\left[x(n)\sin(\omega' t)-IMF_i^j(n)\right]\right\|_2^2 \end{aligned} \tag{12}$$

T_j is the modulation difference operator, which is defined in Equation (8), $\omega' = M\omega$ in which ω is equal to the maximum frequency of $r_i(n)$, $\lambda > 0$ is always set to 1, and $D^{(2)}$ is the second-order difference operator.

(4) use the ACROA to gain the optimal $T_{j(j=1,2,3)}$ to solve L1 problem, and then find the minimum T_j and choose the optimal $IMF_i(n)$ of T_j. The procedure of the method is introduced as follows:

(5) Update $r_i(n)$: $r_{i+1}(n) = r_i(n) - IMF_i(n)$.

(6) If the terminal condition in Equation (13) is achieved, terminate the iteration procedure; otherwise, return to step 3.

$$\|IMF_i(n) - IMF_{i-1}(n)\|_2^2 / \|IMF_{i-1}(n)\|_2^2 \le \varepsilon \tag{13}$$

C. COMPOUND SIMPSON INTEGRAL ALGORITHM

Simpson algorithm is a common integration algorithm. Compared to the dot product sum algorithm in the traditional electric energy measurement, when calculating the parameters such as voltage, current and power in the electric energy measurement, the algorithm has higher algebraic accuracy.

The integral formula with which we are most familiar is the first-order trapezoidal quadrature formula, where $f(x)$ is the integrand function, and $[a, b]$ is the integration interval.

$$I = \int_a^b f(x)dx \approx \frac{b-a}{2}[f(a)+f(b)] \tag{14}$$

The algebraic precision of the quadrature formula is 1. This article uses Simpson quadrature formula with the algebraic precision of 3.

The traditional dot product sum algorithm mainly uses the $P = UI$ formula, first, we sample the signal and calculate the power of a single point, then, we integrate and sum it. The algorithm steps are as follows:

First, apply the integral formula for the voltage and current, where $i(t)$ is the current signal and $u(t)$ is the voltage signal.

$$\begin{aligned} U^2 &= \frac{1}{T}\int_0^T u^2(t)dt = \frac{1}{T}\sum_{k=0}^{n-1}\int_{t_k}^{t_{k+1}} u^2(t)dt\\ &\approx \frac{1}{T}\sum_{k=0}^{n-1} u^2(t_k)\cdot\Delta T = \frac{1}{n}\sum_{k=0}^{n-1} u^2(k) \end{aligned} \tag{15}$$

$$\begin{aligned} I^2 &= \frac{1}{T}\int_0^T i^2(t)dt = \frac{1}{T}\sum_{k=0}^{n-1}\int_{t_k}^{t_{k+1}} i^2(t)dt\\ &\approx \frac{1}{T}\sum_{k=0}^{n-1} i^2(t_k)\cdot\Delta T = \frac{1}{n}\sum_{k=0}^{n-1} i^2(k) \end{aligned} \tag{16}$$

Then, according to $P(t) = u(t) \times i(t)$, use the integral formula for power P:

$$\begin{aligned} P &= \frac{1}{T}\int_0^T p(t)dt = \frac{1}{T}\sum_{i=0}^{n-1}\int_{t_k}^{t_{k+1}} P(t)dt\\ &\approx \frac{1}{T}\sum_{k=0}^{n-1} P(t_k)\cdot\Delta T = \frac{1}{n}\sum_{k=0}^{n-1} P(k) \end{aligned} \tag{17}$$

To find the electric energy in sampling period T, use the following formula:

$$E = \int_0^T P(t)dt = \lim_{\lambda \to 0} \sum_{k=0}^{n-1} P(t_k)\Delta t_k \approx \sum_{k=0}^{n-1} P(k) \cdot \Delta T \quad (18)$$

where λ is the maximum subinterval length; T is the signal period; ΔT is the signal sampling time interval; n is the number of sampling points, E is electric energy.

The dot product sum algorithm uses the traditional integral summation. With this algorithm, it is troublesome to select the number of sampling points, and the number of sampling points must be determined according to the characteristics of the harmonics. In addition, the accuracy of this method is low, especially when we calculate complex DC current signals, large errors will occur. And when the dot product sum algorithm is used in DC energy measurement, the positive error generated will continue to accumulate, unlike the AC energy measurement, which will produce positive and negative errors, the positive and negative errors can cancel each other out. Therefore, the dot product sum algorithm is not suitable for DC energy measurement.

The Simpson integral algorithm is a second-order integral formula, and its formula is as follows:

$$\int_a^b f(x)dx \approx \frac{b-a}{6}[f(a) + 4f(\frac{a+b}{2}) + f(b)] \quad (19)$$

The coefficient of Simpson integral formula is calculated according to Cotes coefficient formula, and its algebraic accuracy is 3, which can better satisfy the accuracy requirements of electric energy measurement.

To further improve the accuracy of the integration algorithm, we perform Simpson formula on multiple intervals to obtain the compound Simpson formula. The steps of the compound Simpson integral algorithm formula are as follows:

First, take N points in sampling period T, divide the period into N time intervals $[t_k, t_{k+1}], = 0, 1 \ldots, \mathrm{N} - 1$ and divide each interval in half, each interval is equally divided into two intervals $[t_{2k}, t_{2k+2}], i = 0, 1 \ldots, \mathrm{N}/2 - 1$. Then, integrate the voltage, current, and power in every two intervals, the formula is as follows:

$$\int_{t_{2i}}^{t_{2i+1}} u^2(t)dt \approx \frac{1}{3} \cdot \frac{T}{N} \cdot \left[u^2(t_{2i}) + 4u^2(t_{2i+1}) + u^2(t_{2i+2})\right] \quad (20)$$

$$\int_{t_{2i}}^{t_{2i+1}} i^2(t)dt \approx \frac{1}{3} \cdot \frac{T}{N} \cdot \left[i^2(t_{2i}) + 4i^2(t_{2i+1}) + i^2(t_{2i+2})\right] \quad (21)$$

$$\int_{t_{2i}}^{t_{2i+1}} P(t)dt \approx \frac{1}{3} \cdot \frac{T}{N} \cdot [P(t_{2i}) + 4P(t_{2i+1}) + P(t_{2i+2})] \quad (22)$$

Because this is a compound integral over two intervals, the coefficient is multiplied by 2 on the original Simpson integral formula.

Then, sum the integrals of the above formula for each interval, and the following formula can be obtained:

$$U^2 = \frac{1}{T}\int_0^T u^2(t)dt = \frac{1}{T}\sum_{i=0}^{\frac{N}{2}-1}\int_{t_{2k}}^{t_{2k+1}} u^2(t)dt \approx \frac{1}{N}\sum_{i=0}^{\frac{N}{2}-1}\frac{1}{3} \cdot \left[u^2(t_{2i}) + 4u^2(t_{2i+1}) + u^2(t_{2i+2})\right] \quad (23)$$

$$I^2 = \frac{1}{T}\int_0^T i^2(t)dt = \frac{1}{T}\sum_{i=0}^{\frac{N}{2}-1}\int_{t_{2k}}^{t_{2k+1}} i^2(t)dt \approx \frac{1}{N}\sum_{i=0}^{\frac{N}{2}-1}\frac{1}{3} \cdot \left[i^2(t_{2i}) + 4i^2(t_{2i+1}) + i^2(t_{2i+2})\right] \quad (24)$$

$$P = \frac{1}{T}\int_0^T p(t)dt = \frac{1}{T}\sum_{i=0}^{\frac{N}{2}-1}\int_{t_{2k}}^{t_{2k+1}} p(t)dt \approx \frac{1}{N}\sum_{i=0}^{\frac{N}{2}-1}\frac{1}{3} \cdot [p(t_{2i}) + 4p(t_{2i+1}) + p(t_{2i+2})] \quad (25)$$

$$E = \int_0^T P(t)dt = \sum_{i=0}^{\frac{N}{2}-1}\int_{t_{2k}}^{t_{2k+1}} P(t)dt \approx \frac{T}{N}\sum_{i=0}^{\frac{N}{2}-1}\frac{1}{3} \cdot [P(t_{2i}) + 4P(t_{2i+1}) + P(t_{2i+2})] \quad (26)$$

The above compound Simpson formula has been widely used in AC electric energy measurement and can be appropriately modified and applied to the DC electric energy measurement.

According to the analysis of the measured signal, there are DC, harmonics, distortion (including broadband signal and narrowband signal) and noise signal in the DC signal. In addition to the noise signal, other signal components are to be calculated. In AC energy measurement, the power calculation of harmonics is $P = UI\cos\theta$, but since there is basically no power factor in the DC signal, the power calculation formula of harmonics is $P = UI$. This article will first use the MBMD algorithm to denoise the DC signal, and then use the complex Simpson integral algorithm for energy measurement.

III. SIMULATION ANALYSIS

A. COMPARISON OF MBMD AND BMD

The advantage of MBMD over BMD is to address square wave signals with strong noise or insufficient signal relative

bandwidth; since the constructed S_2 model is a photovoltaic signal model, there will be almost no case of excessive relative bandwidth. To better distinguish the algorithm of MBMD and BMD, another signal model S_3 with a relatively large bandwidth and strong noise is constructed in this section. $square(\omega n, rate)$ is the signal that defined as square wave, the duty ratio is the rate, and the angular frequency is ω. $x_1(n)$ in Equation (27) consists of a noise signal that signal-to-noise ratio (SNR) is -1, a square wave signal, and the sampling rate is 4 kHz. In Figure 2, we show the mixed signal and its components.

$$x_1(n) = square(30\pi t, 0.5) + n(t) + \sin(30\pi t) \quad (27)$$

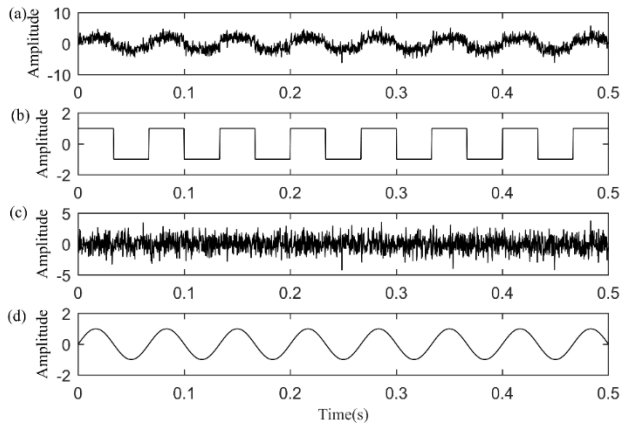

FIGURE 2. Time domain waveform of $x_1(n)$. (a) Mixed signal (SNR = -1); (b) square wave signal; (c) noise signal; (d) sinusoidal.

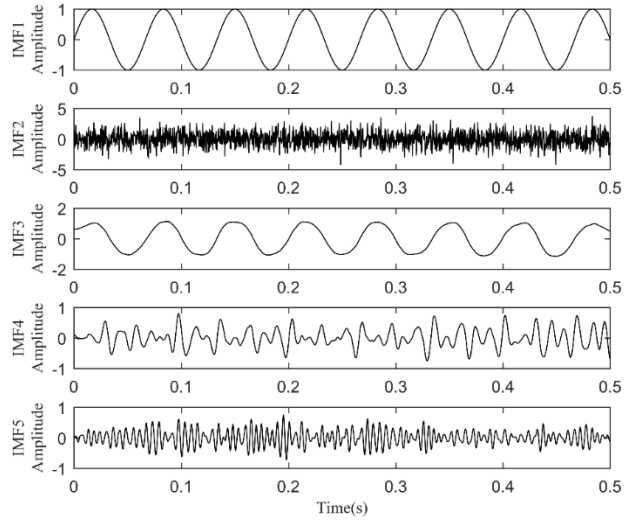

FIGURE 3. $x_1(n)$'s decomposition result generated by BMD.

$x_1(n)$ is decomposed by BMD and MBMD. The result of BMD generation is shown in Figure 3. From the original mixed signal, BMD can separate the sine wave signal (IMF_1) and noise (IMF_2), but the effective square wave signal is decomposed into three narrow-band components, which are IMF_3, IMF_4 and IMF_5, and a noise component. Obviously, IMF_3 is similar to a square wave signal. The decomposition result of MBMD is shown in Figure 4, which is highly consistent with the actual composition. The evaluation parameters of the square wave component of $x_1(n)$and the effective components (IMF_1 of MBMD and IMF_3 of BMD) are shown in Table 1, where r_1 is the correlation coefficient, and E_1 is the energy error. Thus, Table 1 shows that although MBMD runs for a longer time, MBMD obtains more accurate results.

According to the form of Fourier series of the square wave function of Equation (3), the Fourier series of square wave signal in signal $x_1(n)$ can be expressed as follows:

$$square(30\pi n, 0.5) = \sum_{i=1}^{+\infty} \frac{1}{2i-1} \sin[(2i-1) \times 30\pi t] \quad (28)$$

The square wave signal's Fourier series coefficient is $\frac{1}{2i-1}$, and the amplitude will rapidly decrease. Considering the first five components, the square wave signal can be expressed as follows:

$$square(30\pi n, 0.5) \approx \sin(30\pi t) + \frac{1}{3}\sin(90\pi t) + \frac{1}{5}\sin(150\pi t) + \frac{1}{7}\sin(210\pi t) + \frac{1}{9}\sin(270\pi t) \quad (29)$$

Figure 5 shows the comparison of square wave signals generated by BMD and three IMFs' Fourier series in the time domain. In Figure 5, IMF_3, IMF_4 and IMF_5 are compared with $\sin(30\pi t)$, $\frac{1}{3}\sin(90\pi t) + \frac{1}{5}\sin(150\pi t)$ and $\frac{1}{7}\sin(210\pi t) + \frac{1}{9}\sin(270\pi t)$, respectively. The red line represents the theoretical signal, and the black line represents the decomposed IMF component. The black line and red line have a high degree of similarity. Thus, BMD decomposes the square wave component into three narrowband components: IMF_3, IMF_4, and IMF_5. As demonstrated in the theoretical analysis in Chapter 3, Section 2, the BMD algorithm may treat the Fourier series of the square signal as three narrowband components, because the square wave signal is interfered by strong noise. For the MBMD algorithm, it can generate more accurate decomposition results, due to the square wave signal is modulated by a high-frequency signal.

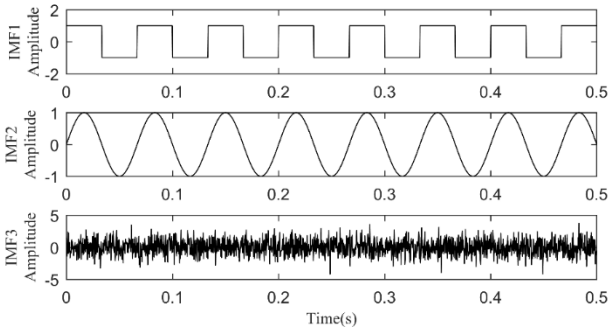

FIGURE 4. $x_1(n)$'s decomposition result generated by MBMD.

B. COMPARISON OF OTHER ALGORITHMS WITH MBMD ALGORITHM

The signal model in this section is photovoltaic signal model S_2 constructed by Equation (3). The simulation experiment

TABLE 1. Evaluation parameters of active ingredients.

Method	r_1	E_1	T(s)
MBMD	0.9990	0.0017	28.0142
BMD	0.9260	0.2348	19.3428

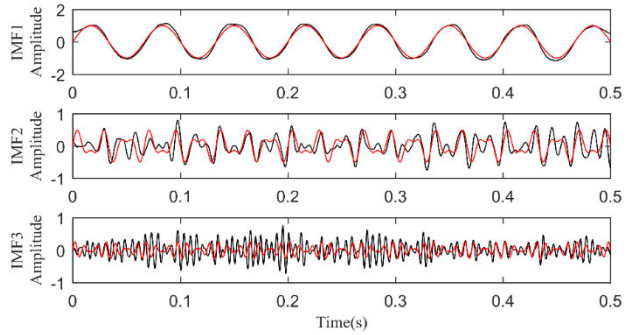

FIGURE 5. Comparison between the actual Fourier series of $x_1(n)$ and IMFs of BMD.

uses the MATLAB experiment platform, the sampling frequency is 2000 Hz, and this signal is shown in Figure 6.

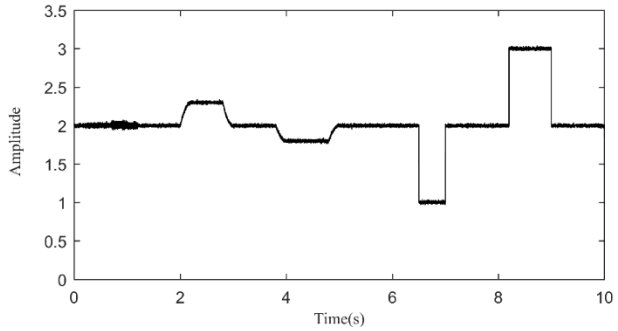

FIGURE 6. S_2 signal model graph.

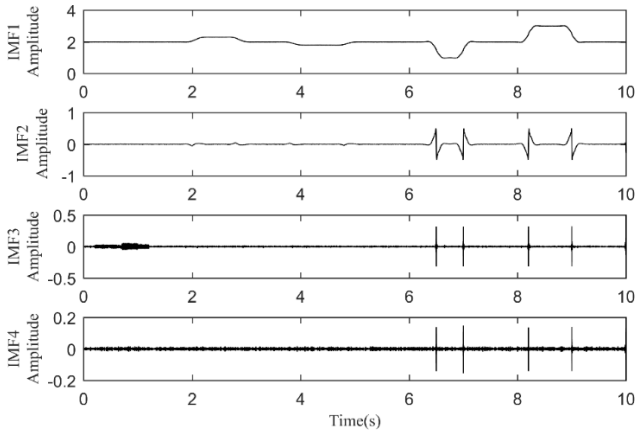

FIGURE 7. S_2 decomposition result generated by VMD.

To facilitate the comparison, we use EEMD, VMD and MBMD to separate S_2 respectively. The decomposition result using the VMD algorithm is shown in Figure 7. The VMD algorithm decomposes S_2 into four components: IMF_1, IMF_2, IMF_3 and IMF_4. There are a series of obvious interference in the figure. IMF_1 is the closest to the original signal, but the corners of its square wave component have obvious sharpening phenomenon because VMD's theory is adaptive filtering, which is affected by Gibbs phenomenon, so sharp corners will appear. Figure 8 illustrates the decomposition result of the EEMD algorithm. Obviously, the useful obtained information is incorrect. Among them, the IMF_3 component is the most similar to the original signal, but the component is very smooth and more like a sinusoidal signal, and its similarity is not as good as the IMF_1 component obtained by the VMD decomposition. Because an interpolation algorithm is used in EEMD algorithm to obtain the extreme envelope, which will produce a smooth IMF component. When calculating the envelope to obtain the IMFs, the final EEMD separation result will become a smooth IMF when we analyze the broadband data set.

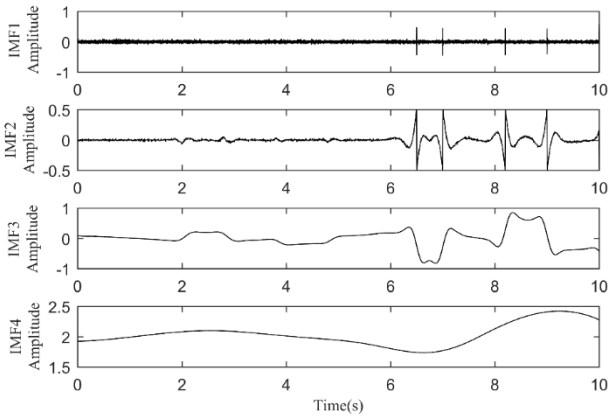

FIGURE 8. Decomposition result of S_2 generated by EEMD.

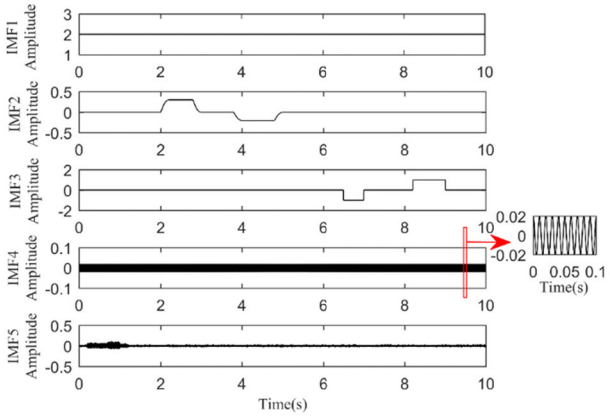

FIGURE 9. S_2's decomposition result generated by MBMD.

Figure 9 shows the decomposition result using the MBMD algorithm. In total, 5 components are obtained: IMF_1, IMF_2, IMF_3, IMF_4 and IMF_5. It can be clearly seen from the figure that each component corresponds to the component of the S_2 signal. IMF_1 is the DC component in the S_2 signal, IMF_2 is the swell and sag component caused when the nonlinear load is connected or disconnected from the circuit,

it is a narrowban9999d component, IMF_3 is the swell and sag component caused by linear load shutdown, which is a square wave component (wideband signal), IMF_4 is the harmonic component generated in the circuit, here is mainly the second harmonic, for the convenience of observation, the small picture next to this component has intercepted the waveform of 0.1s time, and IMF_5 is the noise component. It can be seen that the obtained IMF_3 component does not incur Gibbs phenomenon, and it is highly similar to the square wave component in the original signal.

To make a more accurate comparison, Table 2 lists the accuracy parameters of the separated IMFs obtained by the three algorithms, including the accuracy parameters of energy error E_i, correlation coefficient r_i and time T. Table 2 shows that the IMF obtained by MBMD is closer to the actual square wave component. The separation process was performed on the same computer to compare the calculation time. From the analysis results, the MBMD decomposition has the smallest error and the most accurate decomposition result. However, due to the complex optimization procedures, the MBMD algorithm requires more calculation time than the EEMD and VMD algorithms.

TABLE 2. The generated signal's evaluation parameters.

Method	r_1	E_1	T(s)
VMD	0.9795	0.0114	4.5214
EEMD	0.8233	0.5463	8.9837
MBMD	0.9993	0.0012	33.6251

IV. EXPERIMENTAL ANALYSIS

A. SIGNAL ACQUISITION

From the photovoltaic power metering device's experimental platform of in Figure 10, the experimental photovoltaic data were collected. The experimental platform consists of solar panels, computers, controllers, batteries, signal measurement modules, AD conversion modules, DC loads, AC loads, and inverters. The size of the solar panel is 1480 mm × 680 mm. There are two pieces in total. The battery voltage is 12 V. The inverter is a 12 V,1000 W industrial frequency inverter. The DC load includes the DC linear load (DC bulb) and DC nonlinear load (DC motor)., The AC load also includes the AC linear load (AC bulb) and AC nonlinear load (AC motor). The signal measurement module contains the Hall DC voltage sensor, DC current sensor, AC voltage sensor, and AC current sensor. The signal is collected by the specific collection software on the computer. The signal acquisition frequency is 2 kHz, and the sampling time is 20 s. Figure 11 shows a set of collected front-end and back-end experimental data of the inverter from top to bottom in the order of DC voltage, DC current, AC voltage, and AC current. The DC current and voltage are collected from the inverter to the battery, while the AC voltage and current are collected from the inverter to the AC load. The DC voltage and DC current collect the voltage and current data from the inverter to the battery, while the AC voltage and AC current collect the data from the inverter to the AC load.

Equation (1) and (9), the amplitude of the sinusoidal components is decreased along with the increasement of frequency. Therefore, a general form of the broadband signals can be constructed:

FIGURE 10. Photovoltaic energy metering device experimental platform diagram: ① computer; ② 36 w AC bulb; ③ 10 w AC motor; ④ 28 w AC motor; ⑤ 20.4 w DC motor; ⑥ battery; ⑦ 50 w DC bulb; ⑧ inverter; ⑨ controller; ⑩ signal measurement module; AD conversion module.

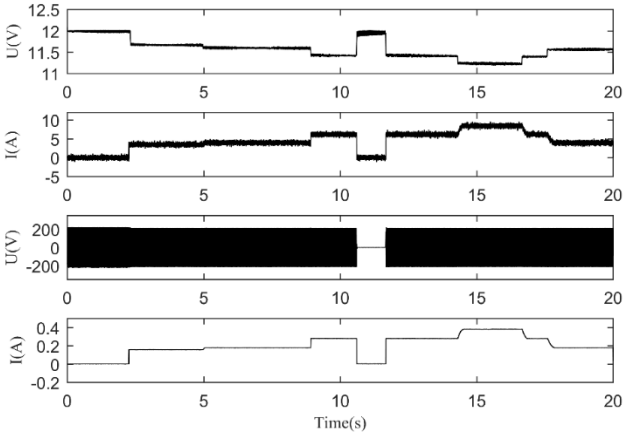

FIGURE 11. Experimental signal graph.

The two current diagrams show, that there are different signal sags and sags caused by the connection and disconnection of linear loads and nonlinear loads within 20 s of collecting signals. The AC voltage is 0 for 10-12 s because the main switch of the AC load is disconnected, so the AC voltage cannot be measured. However, in the period of 0-2 s, the AC current is 0, and the AC voltage is not 0 because the main AC switch is open, but no AC load is open. Therefore, we collected the 220 V AC voltage and 0 A AC current. Although there is no load, there is a slight disturbance in the circuit, the actual collected current signal slightly fluctuates above and below 0 A. Since the DC voltage measures the voltage from the inverter to the battery, it is actually the voltage at both ends of the battery. Regardless of the change

in AC terminal load, the DC terminal voltage will fluctuate at approximately 12 V and will not drop to zero.

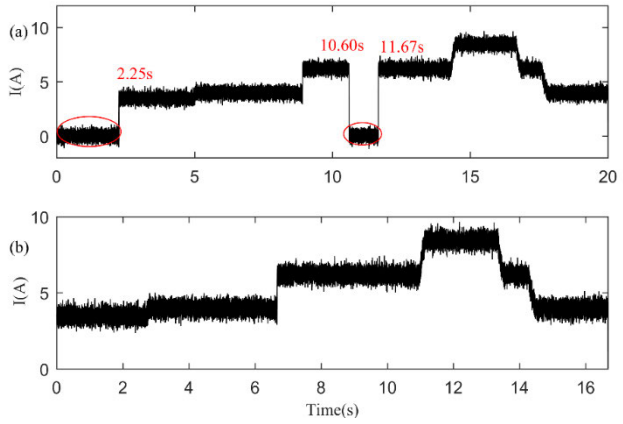

FIGURE 12. DC current graph.

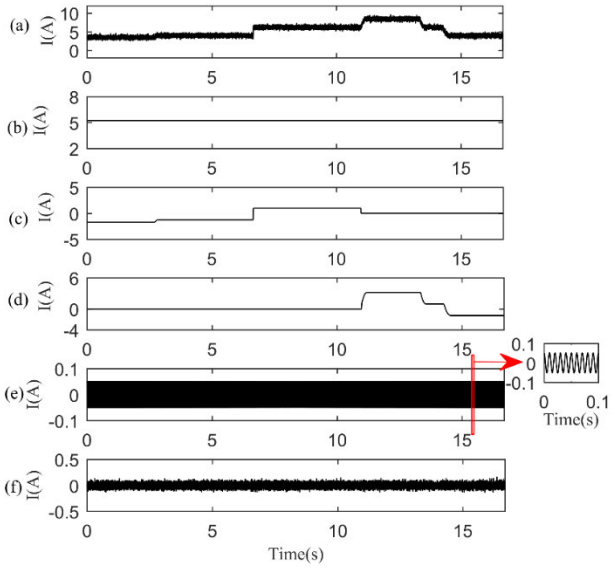

FIGURE 13. MBMD decomposition diagram: (a) DC current signal; (b) DC component; (c) wideband signal; (d) narrowband signal; (e) harmonic signal; (f) noise signal.

B. COMPARISON OF COMPOUND SIMPSON AND DOT PRODUCT SUM

Because the DC current is the most representative of DC signals, the comparison between MBMD and other algorithms is based on the DC current signal collected in Figure 11 as an example. From the point of view of DC current, there are two time periods where the current is 0, and there are only some noise signals. It is meaningless to analyze the signals of these two time periods. Therefore, the signals of these two time periods are deleted, and the remaining signals are combined for electric energy measurement. Although a part of the signal is intercepted, the electric energy of this part is 0, so the total electric energy is unchanged, the average power is $P = E/t$, E does not change, t takes 20s, then the average power obtained will not change. Figure 12 (a) is the original DC current signal. The red ellipses are used to mark the current in the two time periods to be deleted, and the specific time is marked. Figure 12 (b) is the intercepted DC current graph. Figure 13 is the decomposition of the intercepted DC current signal by the MBMD algorithm, (b) is the DC component in the current signal, (c) is the wideband signal, (d) is the narrowband signal, it can be seen from the figure that the signals of (c) and (d) are divided into several segments in the figure. The difference is that at least one end of each segment of the broadband signal contains a sharp corner, the ends of each segment of the narrowband signal are rounded, (e) is a harmonic signal, it can be seen that there are 10 complete sine waveforms within 0.1s, and the frequency of the harmonic is 100Hz, which is exactly twice the power frequency, and it is the second harmonic. In the photovoltaic DC signal, most of the harmonics are the second harmonic, and the other harmonics have less content, (f) is the noise signal.

Before comparing the advantages and disadvantages of the compound Simpson integral algorithm, dot product algorithm and algorithm to calculate the DC signal power, a simple experiment was conducted. The experimental platform is that of the photovoltaic power metering device in Figure 10. Since the AC terminal voltage and current are stable, the DC terminal power can be obtained by dividing the AC terminal power by the inverter conversion efficiency, and we use this power as a standard to measure the accuracy of the compound Simpson integral algorithm and dot product sum algorithm. The conversion efficiency of the inverter is 85%. To verify the actual conversion efficiency of the inverter, we open several different AC loads to make the load work in a stable state. We first measure the power at the AC load (the average power taken here), then, we measure the power at the DC end and compare the two powers to obtain the conversion efficiency of the inverter. Table 3 lists several sets of data measured in this experiment. The conversion efficiency of the inverter is within 85%±0.01%.

TABLE 3. Measured inverter conversion efficiency.

load	AC power	DC power	Conversion efficiency
(36w) AC lights	35.940w	42.278w	85.008%
(6w) AC motor	6.031w	7.095w	85.004%
(28w) AC motor	27.994w	32.936w	84.995%

We perform the MBMD decomposition on the DC current signal, DC voltage signal. Then, we superimpose the effective components and delete unnecessary signals such as noise, to rebuild a new signal, which is conducive to the electrical energy measurement of the system. Figure 14 shows the DC current signal and DC voltage signal after MBMD decomposition, as well as the AC current signal and AC voltage signal without MBMD decomposition, and each signal deletes two meaningless time periods from the original signal. Figure 14(a) is the reconstructed DC current signal

formed by superimposing the signals (b), (c), (d) and (e) of Figure 13 together. Similarly, Figure 14(b) is the DC voltage signal after MBMD decomposition and reconstruction, and Figure 14(c) and (d) are the undecomposed reconstructed AC current and AC voltage signals.

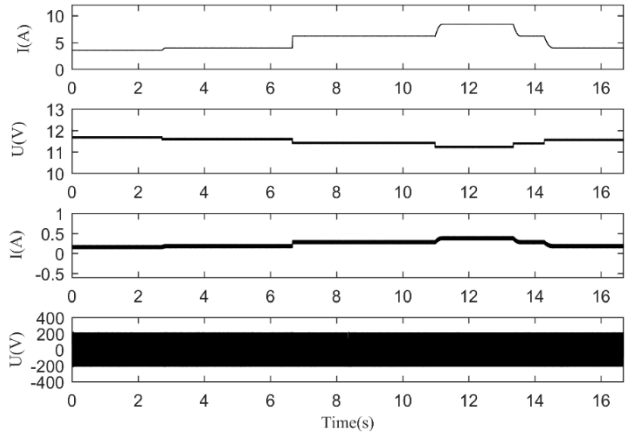

FIGURE 14. The reconstructed signal diagram: (a) reconstructed DC current signal; (b) reconstructed DC voltage signal; (c) reconstructed AC current signal; (d) reconstructed AC voltage signal.

Since the most commonly used algorithm to calculate the AC power is the dot product sum algorithm, and the AC signal is stable, we use the dot product sum for signals (c) and (d) to find that the AC power is $E = 853.500$ J, the average power is $P = E/t = 42.675$ w, and the DC power is $P_1 = P \div \eta = 42.675 \div 0.85 = 50.206$ w. The signal at the DC terminal is decomposed by MBMD, so the comparison of the two integration algorithms is based on the same signal decomposition algorithm. We use P_1 as the standard of DC terminal power to compare the compound Simpson integral algorithm and dot product sum algorithm, as shown in table 4, where E is the electric energy, P is the power, and r is the error. Obviously, the error of using the compound Simpson integral algorithm to find the DC terminal power is smaller, and the accuracy is higher.

TABLE 4. Algorithm parameter comparison.

Algorithm	E	P	r
Compound Simpson	1004.180	50.209	0.003
Dot product sum	1000.960	50.048	0.158

C. VERIFICATION OF THE EFFECTIVENESS OF MBMD ALGORITHM

Since the DC current signal is the most representative, the MBMD algorithm, EEMD algorithm and VMD algorithm are compared by taking the DC current signal in Figure 12 as an example. In Section 4.2, Figure 12 shows the decomposition effect of MBMD on the DC signal. For the convenience of comparison, Figure 15 shows the component (b) of Figure 12, which is the intercepted DC current graph. Figure 16 shows the result of MBMD algorithm decomposition, excluding the component (a) of Figure 13, Figure 17 shows the decomposition diagram of the VMD algorithm, Figure 18 shows the decomposition diagram of the EEMD algorithm, and Figure 16, Figure 17, and Figure 18 are the decomposition results of Figure 15.

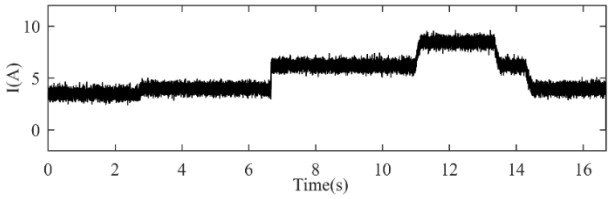

FIGURE 15. DC current graph.

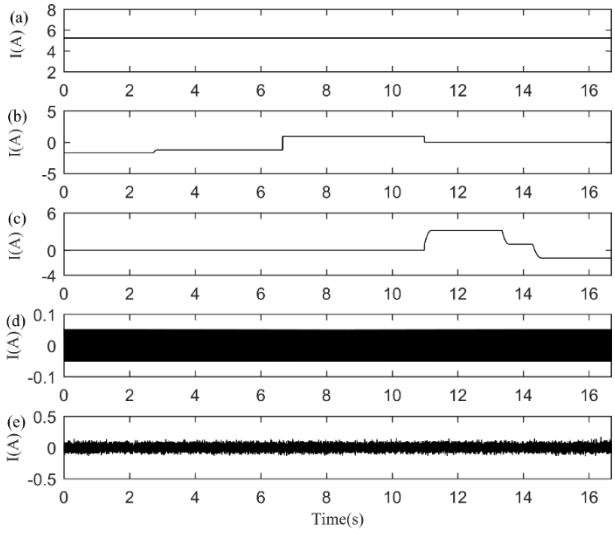

FIGURE 16. MBMD decomposition graph: (a) DC signal; (b) wideband signal; (c) narrowband signal; (d) harmonic signal; (e)noise signal.

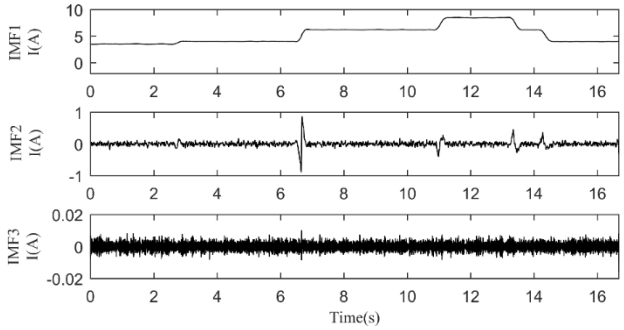

FIGURE 17. VMD decomposition graph.

Both the VMD algorithm and the EEMD algorithm have many IMF components. Some of the multiple IMF components have similar characteristics. Here, the similar components are superimposed together, and three of the IMF components are taken for analysis. Among the three IMF components decomposed by the VMD algorithm, IMF_1 is the closest to the original DC signal, but it can be seen that it

has an obvious Gibbs phenomenon, the characteristics of the broadband signal are not retained, and all sharp corners are separated. The sharp corners appearing in the IMF_2 component are the abrupt features of the distorted signal (wideband signal), and the IMF_3 component is the remaining signal components, including harmonics, noise and some residual abrupt features. Among the three components decomposed by the EEMD algorithm, IMF_1 contains abrupt characteristics, and the IMF_2 component is closest to the original signal. Since EEMD uses an interpolation algorithm to obtain the extreme envelope, the IMF generated by EEMD is completely different from the square wave signal. Because it processes the wideband square wave signal into a sinusoidal signal, the IMF component obtained is relatively smooth, which will cause serious modal confusion. IMF_3 is the remaining signal component, including harmonics, noise and some residual abrupt characteristics. The MBMD algorithm decomposes DC signals, distorted signals (wideband signals and narrowband signals), harmonic components and noise components one by one, and the decomposition effect is very good, and Gibbs phenomenon will not occur.

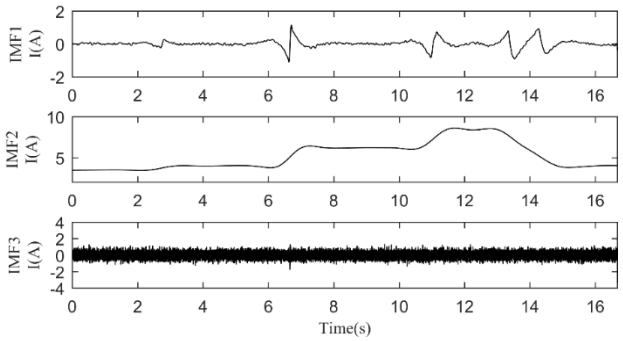

FIGURE 18. EEMD decomposition graph.

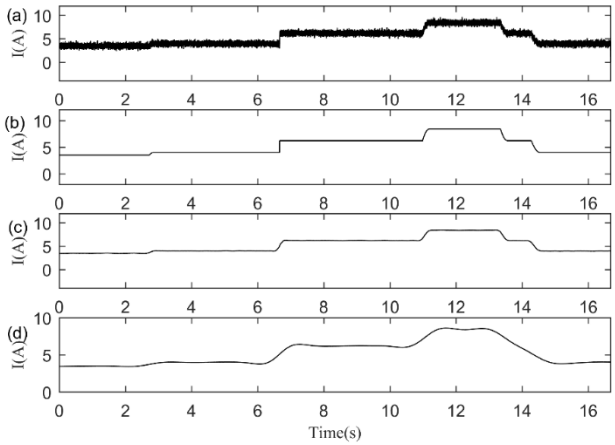

FIGURE 19. Comparison of decomposition effects: (a)DC current signal (b)MBMD reconstruction signal (c)VMD decomposition signal (d)EEMD decomposition signal.

To make a more accurate comparison, Figure 19 combines the other signals except noise component obtained by the MBMD algorithm to form a reconstructed signal, extracts the IMF_1 component of the VMD decomposition diagram and the IMF_2 component of the EEMD decomposition diagram, and compares them with the original DC current signal. It can be seen from Figure 19 that the decomposition effect of the MBMD algorithm is obviously better than the other two algorithms. The characteristics of the square wave signal in the direct current signal containing the square wave signal are retained, and the appearance of the Gibbs phenomenon in the decomposed signal is effectively suppressed.

The previous section compared the compound Simpson integral algorithm and the dot product sum algorithm on the basis of the MBMD decomposition algorithm, and proved the superiority of the compound Simpson integral algorithm. In this section, the original DC terminal signal, MBMD decomposed signal, EEMD decomposed signal and VMD decomposed signal are respectively used to calculate the electric energy by compound Simpson integration algorithm to compare the accuracy and error of different algorithms. The comparison parameters of the three algorithms are listed in Table 5, including the obtained electric energy E, power P, and the absolute error r of the power. The first item in Table 5 is that the original DC signal without any decomposition algorithm uses the complex Simpson integration algorithm. Table 5 shows that MBMD decomposition plus compound Simpson integration algorithm has higher accuracy and smaller error than other algorithms, and can effectively measure DC energy. It can be seen in Table 5 that the MBMD decomposition algorithm combined with the compound Simpson integration algorithm has higher accuracy than other algorithms, with smaller errors, and can effectively measure DC energy.

TABLE 5. Evaluation parameters of the different algorithms.

Method	E	P	r
No Method	1034.287	51.734	1.508
VMD	983.563	49.178	1.028
EEMD	858.234	42.912	7.294
MBMD	1004.180	50.209	0.003

Simulation and experimental analysis results show that MBMD has better accuracy and denoising than the other two methods (EEMD and VMD), and MBMD is better than BMD in addressing the strong noise and insufficient relative bandwidth. In addition, in the experimental analysis, the result calculated by the compound Simpson integral algorithm after the MBMD decomposition is more accurate than the result calculated by other algorithm.

V. CONCLUSION

The photovoltaic DC signal is taken as the research object in this paper. The signal decomposition, signal feature extraction, electric energy measurement for decomposed signal, and a series of algorithm research are performed. A photovoltaic DC power calculation method based on MBMD and complex Simpson integral is proposed.

(1) Due to the deficiencies of the BMD algorithm in dealing with broadband signals whose relative bandwidth

is not small enough, the MBMD algorithm is proposed. The MBMD algorithm multiplies a high-frequency single-frequency component signal as a modulation differential operator to ensure that the relative bandwidth of the signal is far less than 1, which overcomes the shortcomings of the BMD algorithm that the wideband signal is regarded as several narrowband components, resulting in modal confusion. Simulation and experimental results verify the effectiveness of the method. The results show that the method can accurately extract the effective ingredients.

(2) As the dot product sum algorithm is applied to DC energy measurement, the error generated cannot be positive and negative to cancel each other, so the compound Simpson integration algorithm with smaller error and higher accuracy is adopted. Combining the compound Simpson integral algorithm and the MBMD algorithm, a new method of photovoltaic DC signal measurement is proposed. The result shows that this method has higher accuracy of the electric energy measurement. The algorithm can be accurate to at least three decimal places.

(3) Due to the compound optimization process, MBMD is still more time-consuming than VMD and EEMD. Therefore, we will study the rapid optimization method of MBMD in the future.

REFERENCES

[1] P. K. Dash, P. Satapathy, P. Nayak, and M. Sahani, "Islanding and power quality disturbance monitoring in microgrid using adaptive cross variational mode decomposition and reduced kernel ridge regression," *Int. Trans. Electr. Energy Syst.*, vol. 30, no. 6, Jun. 2020, Art. no. e12364.

[2] D. Leite, L. Decker, M. Santana, and P. Souza, "EGFC: Evolving Gaussian fuzzy classifier from never-ending semi-supervised data streams—With application to power quality disturbance detection and classification," in *Proc. IEEE Int. Conf. Fuzzy Syst. (FUZZ-IEEE)*, Jul. 2020, pp. 1–9.

[3] M. Mishra, "Power quality disturbance detection and classification using signal processing and soft computing techniques: A comprehensive review," *Int. Trans. Electr. Energy Syst.*, vol. 29, no. 8, Aug. 2019, Art. no. e12008.

[4] G. T. Heydt and A. W. Galli, "Transient power quality problems analyzed using wavelets," *IEEE Trans. Power Del.*, vol. 12, no. 2, pp. 908–915, Apr. 1997.

[5] S. M. Mousavi Gazafrudi, A. Tabakhpour Langerudy, E. F. Fuchs, and K. Al-Haddad, "Power quality issues in railway electrification: A comprehensive perspective," *IEEE Trans. Ind. Electron.*, vol. 62, no. 5, pp. 3081–3090, May 2015.

[6] P. Ripka, K. Draxler, and R. Styblikova, "Measurement of DC currents in the power grid by current transformer," *IEEE Trans. Magn.*, vol. 49, no. 1, pp. 73–76, Jan. 2013.

[7] A. O. Gur, S. Oksuzer, and E. Karaarslan, "Blockchain based metering and billing system proposal with privacy protection for the electric network," in *Proc. 7th Int. Istanbul Smart Grids Cities Congr. Fair*, Apr. 2019, pp. 204–208.

[8] U. Satija, N. Trivedi, G. Biswal, and B. Ramkumar, "Specific emitter identification based on variational mode decomposition and spectral features in single hop and relaying scenarios," *IEEE Trans. Inf. Forensics Security*, vol. 14, no. 3, pp. 581–591, Mar. 2019.

[9] F. Grimaccia, G. Gruosso, M. Mussetta, A. Niccolai, and R. E. Zich, "Design of tubular permanent magnet generators for vehicle energy harvesting by means of social network optimization," *IEEE Trans. Ind. Electron.*, vol. 65, no. 2, pp. 1884–1892, Feb. 2018.

[10] M.-H. Lee, K.-K. Shyu, P.-L. Lee, C.-M. Huang, and Y.-J. Chiu, "Hardware implementation of EMD using DSP and FPGA for online signal processing," *IEEE Trans. Ind. Electron.*, vol. 58, no. 6, pp. 2473–2481, Jun. 2011.

[11] N. E. Huang, Z. Shen, S. R. Long, M. C. Wu, H. H. Shih, Q. Zheng, N.-C. Yen, C. C. Tung, and H. H. Liu, "The empirical mode decomposition and the Hilbert spectrum for nonlinear and non-stationary time series analysis," *Proc. Roy. Soc. London. A, Math., Phys. Eng. Sci.*, vol. 454, no. 1971, pp. 903–995, Mar. 1998.

[12] B. Pang, G. Tang, and T. Tian, "Enhanced singular spectrum decomposition and its application to rolling bearing fault diagnosis," *IEEE Access*, vol. 7, pp. 87769–87782, 2019.

[13] L. Pang, L. Xu, C. Yuan, X. Li, X. Zhang, W. Wang, X. Guo, Y. Ouyang, L. Qiao, Z. Wang, and K. Liu, "Activation of EGFR-KLF4 positive feedback loop results in acquired resistance to sorafenib in hepatocellular carcinoma," *Mol. Carcinogenesis*, vol. 58, no. 11, pp. 2118–2126, Nov. 2019.

[14] Z. Wang, J. Zhou, J. Wang, W. Du, J. Wang, X. Han, and G. He, "A novel fault diagnosis method of gearbox based on maximum kurtosis spectral entropy deconvolution," *IEEE Access*, vol. 7, pp. 29520–29532, 2019.

[15] Z. Wang, W. Du, J. Wang, J. Zhou, X. Han, Z. Zhang, and L. Huang, "Research and application of improved adaptive MOMEDA fault diagnosis method," *Measurement*, vol. 140, pp. 63–75, Jul. 2019.

[16] Y. Peng, Z. Li, K. He, Y. Liu, Q. Li, and L. Liu, "Broadband mode decomposition and its application to the quality evaluation of welding inverter power source signals," *IEEE Trans. Ind. Electron.*, vol. 67, no. 11, pp. 9734–9746, Nov. 2020.

[17] Y. F. Peng, Z. P. Li, K. F. He, Y. F. Liu, Q. H. Lu, Q. X. Li, L. J. Liu, and R. Q. Luo, "Quality monitoring of aluminum alloy DPMIG welding based on broadband mode decomposition and MMC-FCH," *Measurement.*, vol. 158, Jul. 2020, Art. no. 107683.

[18] K. Dragomiretskiy and D. Zosso, "Variational mode decomposition," *IEEE Trans. Signal Process.*, vol. 62, no. 3, pp. 531–544, Feb. 2014.

[19] K. Yang, G. Wang, Y. Dong, Q. Zhang, and L. Sang, "Early chatter identification based on an optimized variational mode decomposition," *Mech. Syst. Signal Process.*, vol. 115, pp. 238–254, Jan. 2019.

[20] M. Ali, A. Khan, and N. U. Rehman, "Hybrid multiscale wind speed forecasting based on variational mode decomposition," *Int. Trans. Electr. Energy Syst.*, vol. 28, no. 1, p. e2466, Jan. 2018.

[21] S. Mohanty, K. K. Gupta, and K. S. Raju, "Hurst based vibro-acoustic feature extraction of bearing using EMD and VMD," *Measurement*, vol. 117, pp. 200–220, Mar. 2018.

[22] K. T. Sweeney, S. F. McLoone, and T. E. Ward, "The use of ensemble empirical mode decomposition with canonical correlation analysis as a novel artifact removal technique," *IEEE Trans. Biomed. Eng.*, vol. 60, no. 1, pp. 97–105, Jan. 2013.

[23] Z. Feng, M. Liang, Y. Zhang, and S. Hou, "Fault diagnosis for wind turbine planetary gearboxes via demodulation analysis based on ensemble empirical mode decomposition and energy separation," *Renew. Energy*, vol. 47, pp. 112–126, Nov. 2012.

[24] Y. M. Hao, Z. H. Du, Z. X. Xing, and X. H. Mao, "Leakage Signal Analysis of Urban Gas Pipeline Based on Improved Variational Mode Decomposition," *Int. J. Pattern Recognit. Artif. Intell.*, vol. 34, no. 13, pp. 1–22, 2020.

[25] C. Yi, D. Wang, W. Fan, K.-L. Tsui, and J. Lin, "EEMD-based steady-state indexes and their applications to condition monitoring and fault diagnosis of railway axle bearings," *Sensors*, vol. 18, no. 3, p. 704, Feb. 2018.

[26] Y. Li, M. Xu, X. Liang, and W. Huang, "Application of bandwidth EMD and adaptive multiscale morphology analysis for incipient fault diagnosis of rolling bearings," *IEEE Trans. Ind. Electron.*, vol. 64, no. 8, pp. 6506–6517, Aug. 2017.

[27] F. DeRidder, R. Pintelon, J. Schoukens, and A. Verheyden, "Reduction of the gibbs phenomenon applied on nonharmonic time base distortions," *IEEE Trans. Instrum. Meas.*, vol. 54, no. 3, pp. 1118–1125, Jun. 2005.

[28] J. Cheng, Y. Peng, Y. Yang, and Z. Wu, "Adaptive sparsest narrow-band decomposition method and its applications to rolling element bearing fault diagnosis," *Mech. Syst. Signal Process.*, vol. 85, pp. 947–962, Feb. 2017.

[29] Q. Li, Y. Mou, J. Guan, Q. Su, B. Wu, and H. Wu, "Composite simpson method based on differential evolution algorithm for numerical integral," in *Proc. 12th Int. Conf. Natural Comput., Fuzzy Syst. Knowl. Discovery (ICNC-FSKD)*, Aug. 2016, pp. 777–781.

[30] T. Gałaj and A. Wojciechowski, "A study on numerical integration methods for rendering atmospheric scattering phenomenon," *Open Phys.*, vol. 17, no. 1, pp. 241–249, May 2019.

[31] Ç. Dinçkal, "Design of integral spreadsheet calculator for engineering applications," *Comput. Appl. Eng. Educ.*, vol. 26, no. 5, pp. 1159–1172, Sep. 2018.

[32] M. Masjed-Jamei, M. A. Kutbi, and N. Hussain, "Some new estimates for the error of simpson integration rule," *Abstract Appl. Anal.*, vol. 2012, Nov. 2012, Art. no. 239695.
[33] P. J. Elson, "Use of the fast Fourier transform algorithm in the calculation of the operating characteristics of group sequential clinical trials," *Comput. Statist. Data Anal.*, vol. 20, no. 5, pp. 491–498, Nov. 1995.

Z. C. WANG received the B.S. degree from the Hunan University of Science and Technology, Xiangtan, China, in 2019, where he is currently pursuing the master's degree with the College of Mechanical and Electrical Engineering.

His research interests include electrical signal processing and circuit design.

Y. F. PENG (Member, IEEE) received the B.S. degree from Hunan Normal University, Changsha, China, in 2009, and the Ph.D. degree in mechanical engineering from Hunan University, Changsha, in 2017.

He is currently a Lecturer with the Hunan Provincial Key Laboratory of Health Maintenance for Mechanical Equipment, Hunan University of Science and Technology, China. His research interests include signal processing, sparse representation, and pattern recognition.

Y. F. LIU received the B.S. degree from the Hunan University of Arts and Science, China, 2011, and the M.S. degree in mechanical engineering from Hunan University, Changsha, China, in 2014, where she is currently pursuing the Ph.D. degree with the State Key Laboratory of Advanced Design and Manufacturing for Vehicle Body.

Her research interests include signal processing, sparse representation, and machine learning.

K. F. HE received the B.S. and M.S. degrees from the Hunan University of Science and Technology, China, in 2003 and 2006, respectively, and the Ph.D. degree from the South China University of Technology, China, in 2009, all in mechanical engineering.

He is currently a Professor with the School of Mechatronics Engineering, Foshan University, China. His research interests include manufacturing process quality control, in-suit monitoring, signal processing, and structural damage detection.

Z. T. WU was born in Xinxiang, Henan, China, in 1982. He received the B.Sc., M.Sc., and Ph.D. degrees from Hunan University, in 2005, 2008, and 2015, respectively.

He is currently an Associate Professor with Hunan University. His main research interests include dynamic signal analysis and processing and electromechanical equipment monitoring and fault diagnosis.

B. Q. LI was born in Pingyao, Shanxi, China, in 1984.

He currently holds a postdoctoral research position with the State Key Laboratory of Advanced Design and Manufacture for Vehicle Body, School of Mechanical and Vehicle Engineering, Hunan University. His research interests include intelligent health management of mechanical equipment, signal processing, and machine learning.